
FOUNDATION MODEL FOR POLYCRYSTALLINE MATERIAL INFORMATICS

Ting-Ju Wei

Department of Civil Engineering
National Taiwan University
Taipei, Taiwan

Chuin-Shan Chen*

Department of Civil Engineering
Department of Materials Science and Engineering
National Taiwan University
Taipei, Taiwan

December 19, 2025

ABSTRACT

We present a three-dimensional polycrystal foundation model based on a masked autoencoder that learns intrinsic microstructural representations through large-scale self-supervised pretraining on voxel-based data. The pretraining dataset consists of 100,000 face-centered cubic (FCC) microstructures whose crystallographic textures span the texture hull via hierarchical simplex sampling. The quality and transferability of the learned representations are evaluated through two downstream tasks: (i) homogenized stiffness prediction and (ii) nonlinear homogenized response prediction. In the latter, the pretrained encoder is coupled with an orientation-aware interaction-based deep material network (ODMN), where the learned latent representations are used to infer microstructure-dependent ODMN parameters. This enables accurate stress-strain predictions for previously unseen microstructures under crystal plasticity. Across both tasks, the pretrained encoder consistently exhibits superior generalization performance compared to non-pretrained baselines. These results demonstrate the strong transferability of the proposed foundation model and its effectiveness in data-scarce scientific settings with limited labeled microstructures. The framework further enables scalable integration with experimentally derived microstructures, providing a practical basis for microstructure–property reasoning in materials design.

Keywords Foundation model · Crystallographic texture · Microstructural learning · Self-supervised learning · Masked autoencoder · Deep material network · Crystal plasticity

1 Introduction

Polycrystalline materials form the backbone of modern engineering applications, with their macroscopic mechanical behavior intrinsically governed by the underlying microstructural architecture, most notably the crystallographic texture [1]. As a result, elucidating and quantifying microstructure–property relationships has become a central objective in materials design and performance optimization. In recent years, the rapid advancement of artificial intelligence (AI) techniques has opened new avenues for establishing data-driven links between microstructural descriptors and effective material responses, offering a promising route toward accelerated computational materials modeling.

Within this context, a wide range of machine learning architectures have been explored for polycrystalline systems. Convolutional neural networks (CNNs), such as U-Net, have been employed to predict full-field stress distributions in viscoplastic polycrystals [2]. Graph neural networks (GNNs) have demonstrated strong capability in capturing grain-level topological interactions, enabling accurate prediction of effective magnetostriction in heterogeneous polycrystals [3]. Variational autoencoders (VAEs) have been used to learn compact latent representations of electron backscatter diffraction (EBSD) patterns, yielding physically meaningful embeddings that improve EBSD indexing efficiency [4]. More recently, masked autoencoders (MAEs) have been applied to synthetic two-dimensional polycrystalline datasets

*Corresponding author. Email: dchen@ntu.edu.tw

for classification tasks; although the pretraining is restricted to random textured microstructures, the results nevertheless highlight the potential of self-supervised learning for texture-informed representation learning [5]. Collectively, these studies underscore the critical role of latent representation learning in advancing microstructure-aware materials modeling.

Building upon this progress, the concept of a foundation model extends representation learning by leveraging large-scale pretraining on abundant data to extract universal latent representations that are transferable across diverse downstream tasks. In natural language processing, large language models such as BERT and GPT exemplify this paradigm by learning highly generalizable embeddings from massive text corpora [6, 7]. Analogously, foundation models tailored to materials science have begun to emerge. For example, a masked autoencoder pretrained on synthetic two-dimensional composite microstructures has demonstrated strong versatility across downstream tasks, including nonlinear stress-strain response prediction [8].

Motivated by these developments, this study explores the potential of foundation models as a unifying framework for crystallographic texture informatics in polycrystalline materials. To this end, we pretrain a foundation model on a large-scale synthetic dataset that systematically spans the crystallographic texture space. The dataset is constructed using hierarchical simplex sampling (HSS) [9, 10] to traverse the complete texture hull of face-centered cubic (FCC) crystals, thereby capturing the full diversity of crystallographic texture states. Voxel-based polycrystalline microstructures are generated from these sampled textures and used for large-scale self-supervised pretraining.

Building upon this dataset, we develop a three-dimensional voxel-based foundation model for polycrystalline material informatics based on a masked autoencoder architecture, which learns texture-aware latent representations in a self-supervised manner. The pretrained model is subsequently fine-tuned for two representative downstream tasks: (1) prediction of homogenized stiffness, and (2) inference of material surrogate model parameters via a linear projection of the learned latent representations. In the second task, the inferred surrogate parameters are evaluated under crystal plasticity to predict nonlinear homogenized responses. Across both tasks, the pretrained model consistently outperforms non-pretrained baselines, demonstrating strong generalization capability and underscoring the effectiveness of large-scale self-supervised pretraining for texture-aware representation learning.

The remainder of this paper is organized as follows. Section 2 details the proposed methodology, including synthetic dataset generation, foundation model pretraining, and downstream fine-tuning strategies. Section 3 presents and discusses the numerical results for both homogenized stiffness prediction and nonlinear response modeling. Finally, Section 4 summarizes the key findings and outlines perspectives for future developments in foundation model-based approaches for polycrystalline materials.

2 Methods

2.1 Overview of the pretrained dataset

The pretraining dataset is designed to systematically explore the crystallographic texture space of FCC crystals. To this end, it is first necessary to define the sampling space of polycrystalline microstructures in terms of their admissible crystallographic textures. When a texture is represented by an orientation distribution function (ODF), it can be approximated using a discrete basis of Dirac delta functions [11, 12, 13, 9]. In this formulation, the ODF is expressed as

$$f(q) \approx \sum_{j=1}^J p_j \delta(q, q^{(j)}), \quad (1)$$

where $q \in \text{SO}(3)$ denotes the crystallographic orientation, $\delta(\cdot, \cdot)$ is the Dirac delta function defined on the orientation manifold, $q^{(j)}$ represents a discrete set of fundamental orientations obtained from a discretization of $\text{SO}(3)$, and p_j denotes the probability weight associated with each orientation state. In this study, the fundamental orientations are uniformly sampled from the FCC fundamental zone with an angular resolution of 10° , resulting in $J = 618$ discrete orientations in Eq. (1).

The texture coefficients $\{p_j\}$ can be interpreted as probabilistic weights that quantify the likelihood of occurrence of each fundamental orientation. Accordingly, the ODF can be represented in vector form as $\vec{p} = (p_1, p_2, \dots, p_J)$. The convex set spanned by all admissible vectors \vec{p} defines the texture hull M_H [9],

$$M_H = \left\{ \vec{p} \left| 0 \leq p_j \leq 1, \sum_{j=1}^J p_j = 1 \right. \right\}. \quad (2)$$

Each point within the texture hull corresponds to a realizable crystallographic texture. Owing to the high dimensionality of this convex space, an efficient sampling strategy is required to ensure adequate coverage. In this work, HSS is employed to systematically generate representative ODFs by sampling points \vec{p} within the texture hull [9, 10]. A total of 100,000 ODF instances are generated, each representing a distinct crystallographic texture used for constructing the pretraining dataset.

Following ODF generation, each sampled texture is realized as a representative volume element (RVE) using DREAM3D-NX [14]. Each RVE consists of a $45 \times 45 \times 45$ voxel grid containing approximately 810 equiaxed grains. The voxel-wise crystallographic orientations are subsequently reduced to the fundamental zone and converted to quaternion representations to ensure rotational continuity during self-supervised pretraining.

2.2 Self-supervised pretraining stage

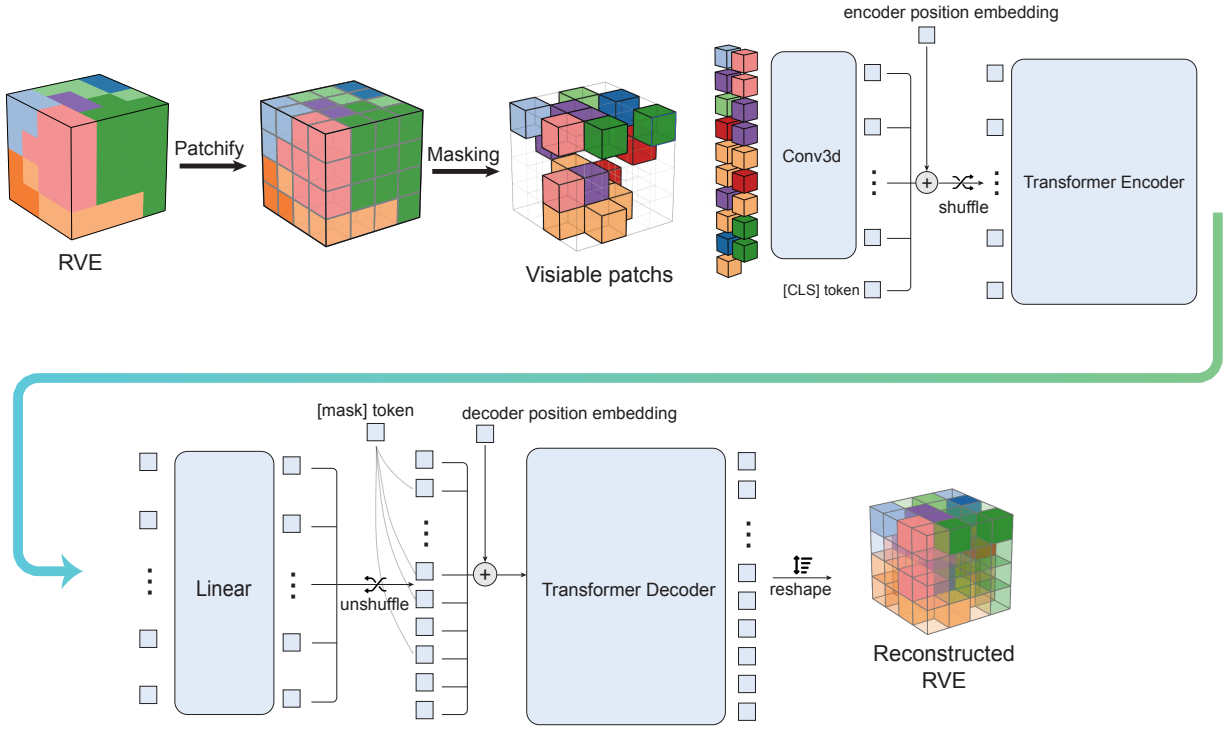


Figure 1: Schematic illustration of the proposed polycrystal foundation model during the self-supervised pretraining stage. The colored voxel grids within the RVE symbolically represent different crystallographic orientations and are shown for illustrative purposes only.

During pretraining, each voxel-based RVE is represented as a four-dimensional tensor of size $(45, 45, 45, 4)$, where the final dimension corresponds to the quaternion components encoding local crystallographic orientations within the fundamental zone. The input tensor is partitioned into non-overlapping cubic patches of size $(\mathcal{P}, \mathcal{P}, \mathcal{P}) = (9, 9, 9)$, yielding $N_p = 125$ patches per training instance. A random subset of patches is masked according to a prescribed masking ratio (e.g., 40%), resulting in 75 visible patches and 50 masked patches.

Each visible patch is mapped into a latent embedding space through a 3D convolutional projection layer with kernel size and stride $(9, 9, 9)$, producing feature vectors of dimension 768. These patch embeddings are then processed by a transformer-based encoder consisting of $\mathcal{N}_e = 12$ blocks, each with an embedding dimension $\mathcal{D}_e = 768$ and $\mathcal{H}_e = 12$ self-attention heads. The encoder outputs compact latent representations that capture texture-aware statistical features of the polycrystalline microstructure.

A lightweight transformer decoder is subsequently employed to reconstruct the masked patches. The decoder comprises $\mathcal{N}_d = 8$ blocks with embedding dimension $\mathcal{D}_d = 512$ and $\mathcal{H}_d = 16$ attention heads. Its role is to infer the quaternion fields of the masked patches from contextual information provided by the visible ones, thereby enforcing spatial and orientational coherence in the reconstructed microstructure.

To encode spatial information, three-dimensional sinusoidal positional encodings (PEs) are added to the inputs of both the encoder and decoder following the formulations in [15, 8]. After patchification, the patch grid has dimensions $\mathcal{G} \times \mathcal{G} \times \mathcal{G}$, with $\mathcal{G} = 5$ in this study. Each spatial coordinate (x, y, z) is independently encoded using sinusoidal functions at multiple frequencies:

$$\begin{aligned} \text{PE}_x^{(2i)}(x) &= \sin\left(\frac{x}{10000^{2i/\mathcal{D}_e}}\right), & \text{PE}_x^{(2i+1)}(x) &= \cos\left(\frac{x}{10000^{2i/\mathcal{D}_e}}\right), \\ \text{PE}_y^{(2i)}(y) &= \sin\left(\frac{y}{10000^{2i/\mathcal{D}_e}}\right), & \text{PE}_y^{(2i+1)}(y) &= \cos\left(\frac{y}{10000^{2i/\mathcal{D}_e}}\right), \\ \text{PE}_z^{(2i)}(z) &= \sin\left(\frac{z}{10000^{2i/\mathcal{D}_e}}\right), & \text{PE}_z^{(2i+1)}(z) &= \cos\left(\frac{z}{10000^{2i/\mathcal{D}_e}}\right), \end{aligned} \quad (3)$$

where $i = 0, 1, \dots, \mathcal{D}_e/2 - 1$.

In addition, a learnable classification token, denoted as [CLS], is prepended to the embedded patch sequence prior to transformer encoding. This token aggregates global microstructural information through the self-attention mechanism. Its positional encoding is set to zero, $\text{PE}_{[\text{CLS}]} = \mathbf{0}$. The complete positional encoding applied to the encoder input is therefore given by

$$\text{PE}_{\text{encoder}} = \text{stack}(\text{PE}_{[\text{CLS}]}, \{\text{concat}(\text{PE}_x(x), \text{PE}_y(y), \text{PE}_z(z)) \mid (x, y, z)\}) \in \mathbb{R}^{(1+N_p) \times \mathcal{D}_e} \quad (4)$$

This asymmetric encoder–decoder architecture mitigates shortcut learning and compels the network to infer high-level statistical dependencies between visible and masked regions of the microstructure. The pretraining objective minimizes the mean squared error (MSE) between the reconstructed quaternion fields $\hat{\mathbf{Q}}_{\text{masked}}^{(i)}$ and the corresponding ground-truth fields $\mathbf{Q}_{\text{masked}}^{(i)}$ within the masked patches. Each patch has a feature dimensionality $d = \mathcal{P} \times \mathcal{P} \times \mathcal{P} \times C$, where C denotes the number of quaternion components. The pretraining loss is defined as

$$\mathcal{L}_{\text{pretrain}} = \frac{1}{|\mathcal{M}|} \sum_{i \in \mathcal{M}} \frac{1}{d} \left\| \hat{\mathbf{Q}}_{\text{masked}}^{(i)} - \mathbf{Q}_{\text{masked}}^{(i)} \right\|_2^2, \quad (5)$$

where \mathcal{M} denotes the set of masked patch indices. This objective enforces accurate reconstruction of the masked quaternion fields, thereby guiding the model to learn meaningful microstructural representations that are essential for downstream tasks.

2.3 Downstream training

Following self-supervised pretraining, the encoder is transferred to downstream tasks and fine-tuned in an end-to-end manner for task-specific objectives. In this stage, the pretrained encoder serves as a microstructure feature extractor, while lightweight task-specific heads are introduced to adapt the learned latent representations to different prediction targets. Specifically, the learnable [CLS] token is employed as the global latent descriptor of the microstructure and is connected to a linear prediction head for the downstream tasks considered in this study.

2.3.1 Downstream task I: Homogenized stiffness prediction

In polycrystalline materials, the homogenized mechanical response is predominantly governed by the underlying crystallographic texture, which dictates the collective anisotropy arising from the orientation distribution of constituent grains. This downstream task is designed to evaluate whether the latent representations learned during self-supervised pretraining can be effectively transferred to predict homogenized elastic properties.

Specifically, the model is tasked with predicting three principal components of the homogenized stiffness tensor, namely \bar{C}_{1111} , \bar{C}_{2222} , and \bar{C}_{3333} , which correspond to the normal elastic moduli along the three orthogonal sample axes. Accurate prediction of these components provides a direct measure of the ability of the pretrained latent representations to map crystallographic texture information to effective macroscopic mechanical responses.

As illustrated in Fig. 2, the pretrained 3D convolutional projection layer and transformer-based encoder are initialized from the pretraining stage and jointly fine-tuned during downstream training. The [CLS] token, which aggregates global microstructural information through the self-attention mechanism, serves as the latent representation of the RVE. A lightweight linear regression head is appended to this token to map the latent features to the target stiffness components.

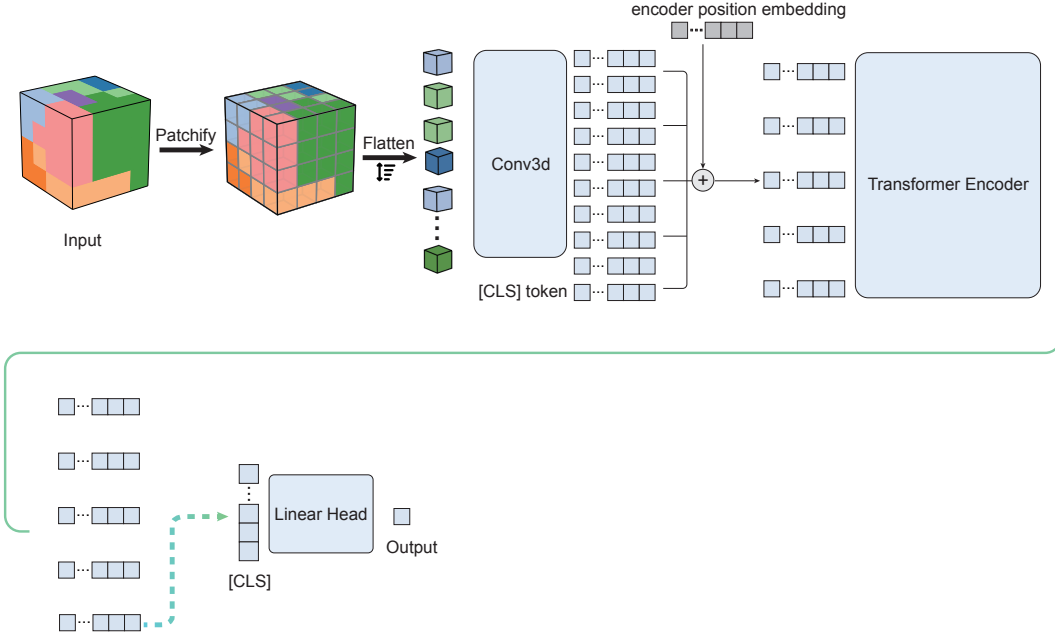


Figure 2: Schematic illustration of the downstream workflow for homogenized stiffness prediction. The pretrained encoder extracts texture-aware latent representations, which are subsequently mapped to homogenized stiffness components through a linear regression head.

For downstream evaluation, a total of 5,000 ODFs are sampled from the texture hull using the HSS algorithm described in Section 2.1, ensuring adequate coverage of the crystallographic texture space. Each ODF is realized as a voxel-based RVE using DREAM3D-NX, consisting of approximately 810 equiaxed grains discretized on a $45 \times 45 \times 45$ voxel grid. The dataset is randomly split into 80% for training and 20% for validation to maintain balanced statistical coverage across the texture space. Homogenized stiffness tensors are computed using the DAMASK-FFT solver [16] under periodic boundary conditions. Each grain is modeled as a single crystal with cubic elastic symmetry, characterized by the elastic stiffness constants listed in Table 1.

Table 1: Elastic stiffness constants of the cubic single crystal used in the downstream DAMASK-FFT simulations.

C_{11} (GPa)	C_{12} (GPa)	C_{44} (GPa)
107.3	60.8	28.3

2.3.2 Overview of the ODMN

Accurately predicting the nonlinear mechanical response of RVEs remains a long-standing challenge, particularly in industrial applications where direct full-field simulations are computationally prohibitive. To address this challenge, the orientation-aware interaction-based deep material network (ODMN) is proposed as an efficient and physically interpretable surrogate modeling framework [17]. The ODMN constitutes an extension of the deep material network (DMN) architecture [18, 19, 20], and is specifically tailored for polycrystalline materials to explicitly incorporate crystallographic texture effects.

Conceptually, the ODMN can be interpreted as a parameterized reduced-order microstructure that approximates the homogenized mechanical response of the original RVE [21, 22]. Starting from a unit cell Ω , the reduced-order microstructure is hierarchically partitioned into 2^N subdomains,

$$\Omega = \bigcup_{i=0}^{2^N-1} \Omega_i, \quad (6)$$

where each subdomain Ω_i corresponds to a material node \mathcal{M}^i in the network. Here, N is a user-defined hyperparameter that controls the resolution of the reduced-order representation, with larger values of N enabling a richer approximation of the RVE homogenized response.

The hierarchical partitioning is encoded through a binary-tree material network of depth N . At each internal tree node located at level l and position p , an interaction direction $\vec{\mathbf{N}}_p^l$ is introduced to characterize the interface orientation governing stress equilibrium between the two adjacent subdomains. At each leaf-level material node \mathcal{M}^i , a set of parameters $\{z^i, \alpha^i, \beta^i, \gamma^i\}$ is assigned, representing the volume fraction and the local crystallographic orientation associated with subdomain Ω_i .

The interaction direction $\vec{\mathbf{N}}$ is parameterized by two angular variables, θ and ϕ , which define a unit normal vector according to

$$\vec{\mathbf{N}} = \begin{bmatrix} \cos(2\pi\phi) \sin(\pi\theta) \\ \sin(2\pi\phi) \sin(\pi\theta) \\ \cos(\pi\theta) \end{bmatrix}. \quad (7)$$

For an ODMN of depth N , the complete set of trainable parameters can be expressed as

$$\begin{aligned} \mathcal{F} = & \{z^i, \alpha^i, \beta^i, \gamma^i \mid i = 0, 1, \dots, 2^N - 1\} \\ & \cup \{\theta_p^l, \phi_p^l \mid l = 0, 1, \dots, N - 1, p = 0, 1, \dots, 2^l - 1\}, \end{aligned} \quad (8)$$

where the first set corresponds to the material-node parameters associated with the reduced subdomains, and the second set specifies the interaction directions at each tree node of the hierarchical material network.

A distinctive feature of the ODMN, inherited from the DMN framework, is that the network can be trained in an offline stage using only linear elastic stiffness data, while still being capable of performing nonlinear mechanical extrapolation during the online prediction stage [18, 23, 19, 24].

This remarkable mechanical extrapolation capability originates from the fact that the ODMN parameters learned during offline training encode a first-order approximation of the microstructural mechanical response under linear elasticity. During online prediction, this first-order approximation is preserved and embedded within the hierarchical homogenization operators, thereby enabling physically consistent extrapolation to nonlinear mechanical behavior [23].

During the online prediction stage, the ODMN performs a downscaling operation from the macroscopic deformation gradient $\bar{\mathbf{F}}$ to the deformation gradient \mathbf{F}^i associated with each subdomain Ω_i according to

$$\mathbf{F}^i = \bar{\mathbf{F}} + \sum_{j=0}^{2^N-2} \alpha^{i,j} \mathbf{a}^j \otimes \mathbf{N}^j, \quad i = 0, 1, \dots, 2^N - 1, \quad (9)$$

where the interaction coefficients $\alpha^{i,j}$ and the corresponding interaction directions \mathbf{N}^j are determined by the network parameter set \mathcal{F} .

At each material node, the local constitutive response is evaluated through the material law

$$\mathbf{P}^i, \frac{\partial \mathbf{P}^i}{\partial \mathbf{F}^i} = \mathbb{P}^i(\mathbf{F}^i, \psi^i), \quad (10)$$

where \mathbf{P}^i denotes the first Piola–Kirchhoff stress of subdomain Ω_i , $\partial \mathbf{P}^i / \partial \mathbf{F}^i$ is the corresponding consistent tangent operator, and $\mathbb{P}^i(\cdot)$ represents the local material law parameterized by the internal state variables ψ^i (e.g., history-dependent variables in crystal plasticity).

The resulting local stresses and tangents are subsequently upscaled through the hierarchical network structure to recover the homogenized first Piola–Kirchhoff stress $\bar{\mathbf{P}}$ and its consistent tangent $\partial \bar{\mathbf{P}} / \partial \bar{\mathbf{F}}$.

The interaction vectors \mathbf{a}^j introduced in Eq. (9) represent fluctuation fields associated with the interfaces between adjacent subdomains in the reduced-order microstructure. During each Newton–Raphson iteration of the online prediction stage, the interaction vectors are initialized as $\mathbf{a}^j = \mathbf{0}$. After evaluating the local constitutive responses at the material nodes, the consistency of the downscaled and upscaled responses is assessed through the Hill–Mandel condition, which requires

$$\left(\sum_{i=0}^{2^N-1} W^i \mathbf{P}^i \alpha^{i,j} \right) \cdot \mathbf{N}^j = 0, \quad j = 0, \dots, 2^N - 2, \quad (11)$$

where W^i denotes the volume fraction associated with subdomain Ω_i .

If the Hill–Mandel condition is violated, the interaction vectors \mathbf{a}^j are updated via a Newton–Raphson procedure, and the downscaling–local evaluation–upscaling cycle is repeated until convergence is achieved. Upon convergence, the homogenized first Piola–Kirchhoff stress $\bar{\mathbf{P}}$ and its consistent tangent $\partial\bar{\mathbf{P}}/\partial\bar{\mathbf{F}}$ are obtained and used to define the macroscopic constitutive response. Further details can be found in the original ODMN formulation [17].

Similar to the original DMN architecture, the ODMN exhibits an inherent limitation in that its parameters are tied to a specific microstructural realization, thereby restricting transferability across different microstructures. To address this limitation, several recent studies have proposed strategies to generalize DMN parameters through interpolation schemes or machine-learning-based frameworks. For example, Huang et al. [25] developed an interpolation-based scheme to predict DMN parameters for previously unseen microstructures. In contrast, Jean et al. [26] employed graph neural networks (GNNs) to infer DMN parameters directly from mesh-based microstructural representations. Wu et al. [27] utilized convolutional neural networks (CNNs) to map two-dimensional microstructural images into a latent feature space, followed by a feedforward neural network to predict the corresponding DMN parameters. More recently, Wei et al. [8] demonstrated that foundation models pretrained on large-scale short-fiber composite images can serve as universal feature extractors, whose learned latent representations are subsequently mapped to DMN parameters.

Nevertheless, the extension of such approaches to three-dimensional polycrystalline microstructures, particularly for mapping learned representations to ODMN parameters, remains largely unexplored. Motivated by this gap, the present study investigates how a foundation model can act as a latent feature extractor for polycrystalline microstructures, whose learned representations are subsequently mapped to surrogate models, such as the ODMN, to enable generalization across diverse microstructural configurations.

2.3.3 Downstream task II: Nonlinear homogenized response prediction

Beyond homogenized stiffness prediction, the second downstream objective extends the pretrained encoder toward nonlinear homogenized response prediction by predicting the parameters of the ODMN [17]. The predicted ODMN parameters are subsequently used to evaluate nonlinear stress–strain responses. This downstream task assesses whether the learned latent representations can be transferred from linear elastic property prediction to the more challenging task of surrogate model parameter prediction.

In this work, voxel-based RVEs are used as inputs to the pretrained 3D convolutional and transformer-based encoder. A linear regression head is appended to the [CLS] token to predict the parameters of the ODMN, as illustrated in Fig. 3(a). The ODMN employed as the surrogate model in this study uses a network depth of $N = 6$, resulting in a total of $|\mathcal{F}| = 382$ parameters. The end-to-end downstream learning process can be expressed as

$$(\mathbf{Q}) \xrightarrow{\mathcal{M}_{\text{FM}}(\mathbf{Q})} (\mathcal{F}, \mathbf{C}^{\text{crystal}}) \xrightarrow{\mathcal{H}_{\text{ODMN}}(\mathcal{F}, \mathbf{C}^{\text{crystal}})} \bar{\mathbf{C}}, \quad (12)$$

where \mathbf{Q} denotes the quaternion field of the voxel-based microstructure with dimensions $(45, 45, 45, 4)$. The mapping \mathcal{M}_{FM} represents the pretrained encoder equipped with a linear regression head, whose trainable parameters are optimized during fine-tuning to predict the ODMN parameter set \mathcal{F} . Given the predicted \mathcal{F} and the single-crystal stiffness tensor $\mathbf{C}^{\text{crystal}}$, the analytical homogenization operator $\mathcal{H}_{\text{ODMN}}$ is then employed to compute the homogenized stiffness tensor $\bar{\mathbf{C}}$. This homogenized stiffness serves as the model output used to define the training loss, which is backpropagated through $\mathcal{H}_{\text{ODMN}}$ to update the parameters of \mathcal{M}_{FM} during downstream fine-tuning.

Specifically, the downstream training objective is defined as the relative Frobenius norm error between the ODMN-predicted homogenized stiffness and the corresponding ground-truth obtained from direct numerical simulation (DNS),

$$\mathcal{L}_{\text{ODMN}} = \frac{1}{N_{\text{dataset}}} \sum_{s=1}^{N_{\text{dataset}}} \frac{\|\bar{\mathbf{C}}_s^{\text{DNS}} - \bar{\mathbf{C}}_s(\mathbf{C}_s^{\text{p1}}, \mathcal{F}_{\text{ODMN}})\|_{\text{F}}}{\|\bar{\mathbf{C}}_s^{\text{DNS}}\|_{\text{F}}}, \quad (13)$$

where N_{dataset} denotes the total number of training samples, and $\|\cdot\|_{\text{F}}$ is the Frobenius norm.

During the online prediction stage, previously unseen microstructures are first processed by the trained mapping \mathcal{M}_{FM} to predict the corresponding ODMN parameter set \mathcal{F} . The predicted \mathcal{F} defines a standalone ODMN, which is subsequently combined with the constituent phase material behavior, such as crystal plasticity, to evaluate the nonlinear mechanical response, as illustrated in Fig. 3(b). This strategy enables efficient prediction of nonlinear mechanical behavior in complex polycrystalline microstructures, while preserving the physical consistency of the underlying multiscale framework.

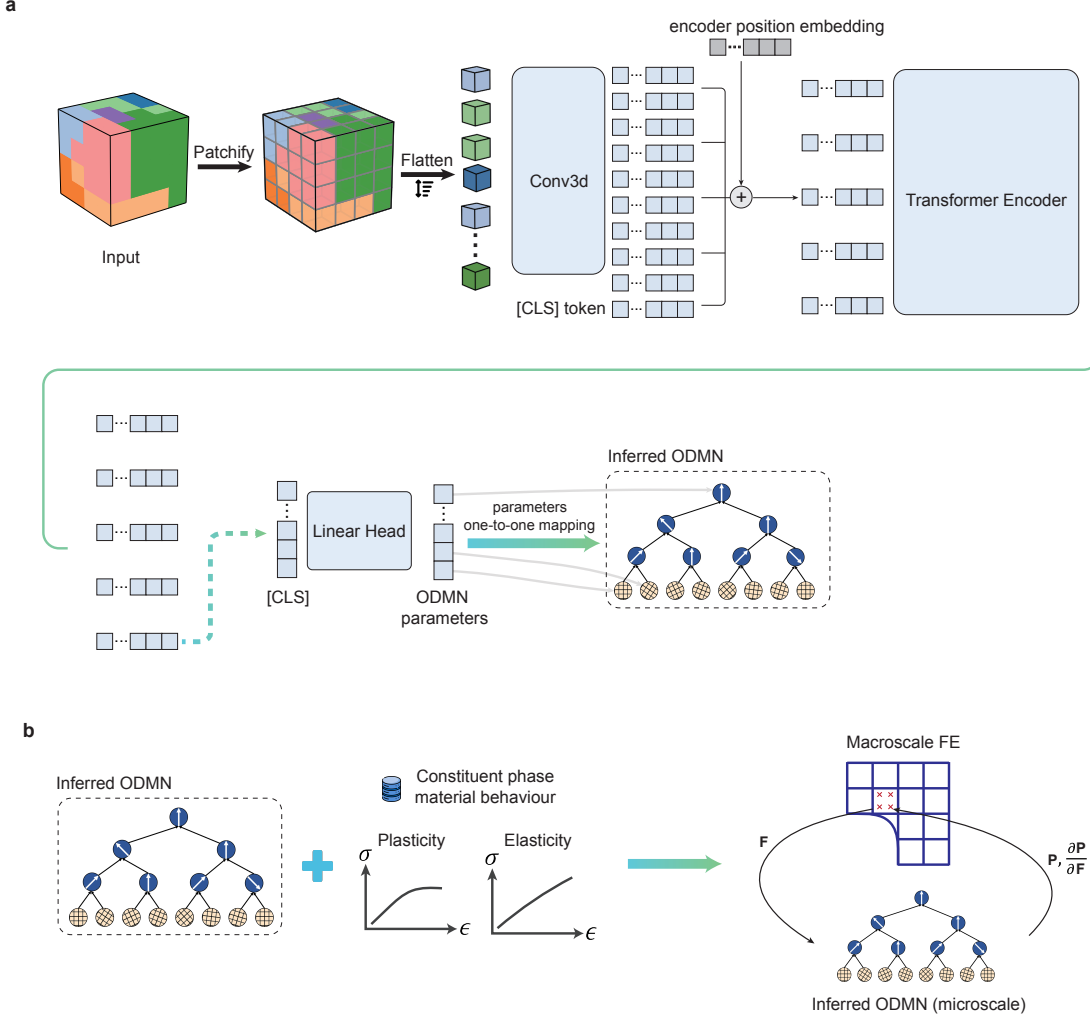


Figure 3: Schematic illustration of the downstream workflow for nonlinear homogenized response prediction. (a) During the downstream offline training stage, the pretrained encoder extracts texture-aware latent features, which are subsequently passed through a linear regression head to predict the ODMN parameters. (b) During the online prediction stage, the inferred ODMN is coupled with the constituent phase material behavior to enable nonlinear homogenized response prediction.

2.3.4 Dataset construction for downstream task II: Nonlinear response modeling

For the second downstream task, a labeled dataset was constructed to enable supervised training for ODMN parameter prediction. Following the strategy proposed by Dai et al. [28], a total of 1,600 polycrystalline microstructures were generated, comprising four representative crystallographic texture types with 400 samples per texture category.

For each microstructure, 500 distinct sets of single-crystal elastic stiffness parameters were generated to enrich the dataset and to cover a wide range of mechanical responses. The dataset was randomly partitioned into training and validation subsets, with 320 and 80 microstructures per texture type assigned to the training and validation sets, respectively.

For each crystallographic texture instance, DREAM3D-NX was employed to generate representative volume elements (RVEs) consisting of approximately 809 equiaxed grains, discretized on a $45 \times 45 \times 45$ voxel grid. The four representative texture types considered in this study are summarized as follows:

- (i) Strong-textured-1: One dominant orientation with $Weight = 500,000$ and $Sigma = 1$; all other orientations are assigned $Weight = 1$ and $Sigma = 1$.

- (ii) Strong-textured-2: One dominant orientation with $Weight = 500,000$ and $Sigma = 8$; all other orientations are assigned $Weight = 1$ and $Sigma = 1$.
- (iii) Weak-textured-1: All orientations are uniformly assigned $Weight = 1$ and $Sigma = 1$, corresponding to a nearly random texture.
- (iv) Weak-textured-2: Two dominant orientations, each with $Weight = 500,000$ and $Sigma = 10$; all other orientations are assigned $Weight = 1$ and $Sigma = 1$.

It is worth noting that the four texture types considered in this study represent a subset, rather than an exhaustive coverage, of the texture hull. They are intentionally selected to capture polycrystalline microstructures with distinct texture intensities and orientation dispersions, thereby providing a controlled yet representative testbed for downstream task.

After RVE realization, each microstructure is paired with 500 distinct single-crystal stiffness triplets $\{C_{11}^{\text{crystal}}, C_{12}^{\text{crystal}}, C_{44}^{\text{crystal}}\}$, which together define the cubic single-crystal stiffness tensor $\mathbf{C}^{\text{crystal}}$ used in Eq. (12):

$$\mathbf{C}^{\text{crystal}} = \begin{bmatrix} C_{11}^{\text{crystal}} & C_{12}^{\text{crystal}} & C_{12}^{\text{crystal}} & 0 & 0 & 0 \\ C_{12}^{\text{crystal}} & C_{11}^{\text{crystal}} & C_{12}^{\text{crystal}} & 0 & 0 & 0 \\ C_{12}^{\text{crystal}} & C_{12}^{\text{crystal}} & C_{11}^{\text{crystal}} & 0 & 0 & 0 \\ 0 & 0 & 0 & C_{44}^{\text{crystal}} & 0 & 0 \\ 0 & 0 & 0 & 0 & C_{44}^{\text{crystal}} & 0 \\ 0 & 0 & 0 & 0 & 0 & C_{44}^{\text{crystal}} \end{bmatrix}. \quad (14)$$

The sampling strategy for the stiffness triplets $\{C_{11}^{\text{crystal}}, C_{12}^{\text{crystal}}, C_{44}^{\text{crystal}}\}$ follows the procedure detailed in the original ODMN study [17], ensuring sufficient variability in the elastic anisotropy of the constituent single-crystal phases. For each pair of microstructure and single-crystal stiffness tensor, the corresponding homogenized stiffness tensor $\bar{\mathbf{C}}^{\text{DNS}}$ is computed using the DAMASK-FFT solver [16].

3 Results and Discussion

3.1 Pretraining performance and latent representation analysis

During the pretraining stage, the foundation model is optimized in a self-supervised manner by randomly masking a subset of the voxel-based microstructure and reconstructing the missing regions. The masking ratio thus constitutes a critical hyperparameter, as it directly controls both the difficulty of the reconstruction task and the amount of microstructural information available to the encoder.

To systematically assess its influence, an ablation study was conducted in which the masking ratio was varied from 20% to 90%, while all configurations were trained for 1400 epochs. As shown in Fig. 4, all training curves exhibit monotonic decay and stable convergence, indicating well-behaved optimization dynamics across the entire range of masking ratios. The final reconstruction error increases consistently with increasing masking ratio. This trend is expected, since higher masking ratios reduce the number of visible patches and consequently limit the microstructural information that can be exploited during reconstruction. Accordingly, the lower reconstruction errors observed at small masking ratios should be attributed to increased information availability rather than interpreted as evidence of a more expressive latent representation.

These observations highlight that reconstruction loss alone is insufficient for assessing representation quality. A more informative evaluation requires examining how effectively the learned latent space transfers to downstream tasks, where the ability to encode texture-sensitive and physically meaningful microstructural features becomes critical. Downstream performance therefore provides a more practically relevant measure of the robustness of the pretrained encoder than reconstruction accuracy achieved during pretraining.

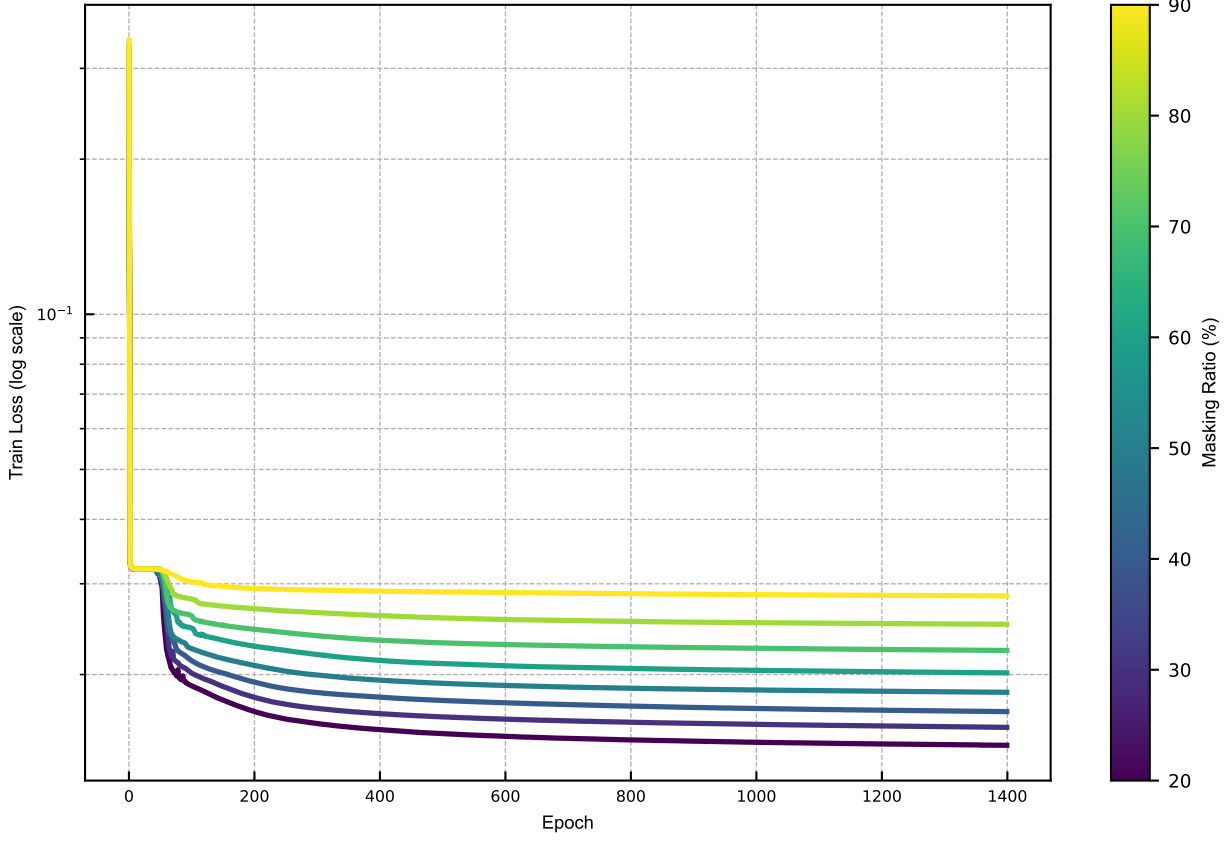


Figure 4: Pretraining loss curves for different masking ratios ranging from 20% to 90%.

Furthermore, the pretraining dataset was generated by sampling the texture hull using the HSS algorithm, which provides broad and diverse coverage of the high-dimensional crystallographic texture space. Under this sampling strategy, a pretrained encoder that is both texture-aware and unbiased with respect to the data distribution is expected to produce a latent representation whose global distribution exhibits no artificial clustering or preferential concentration arising from the pretraining procedure itself.

To examine this behavior, the [CLS] token extracted from the pretrained encoder with a masking ratio of 40% at epoch 1400 was adopted as the latent descriptor for each RVE in the pretraining dataset. These latent vectors were subsequently projected onto a two-dimensional manifold using UMAP for visualization [29]. As shown in Fig. 5, the resulting latent distribution appears broadly and smoothly distributed, without evident clustering or collapse into localized regions. This observation indicates that the pretrained encoder maps the diverse set of crystallographic textures into a well-spread latent space, preserving continuity across the dataset.

Such a smoothly populated latent space suggests that the encoder avoids degenerative representations and maintains sufficient expressiveness to accommodate texture variability. This property is particularly important for downstream transfer, where interpolation within the latent space is expected to correspond to meaningful variations in microstructural and texture-related features.

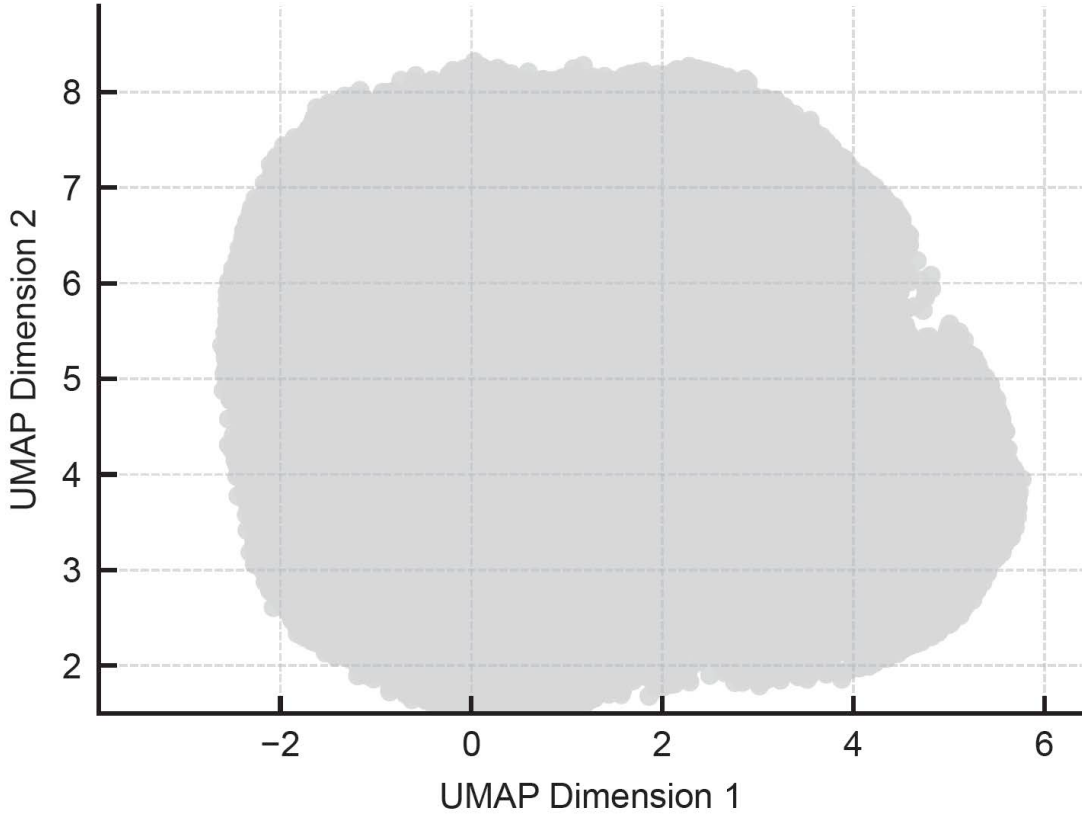


Figure 5: UMAP projection of the latent representations extracted from the pretrained encoder (masking ratio 40%). Each gray point corresponds to a single RVE from the pretraining dataset.

3.2 Downstream task I: stiffness prediction performance

This downstream task evaluates the transferability of the pretrained encoder by predicting the three principal components of the homogenized stiffness tensor, \bar{C}_{1111} , \bar{C}_{2222} , and \bar{C}_{3333} . To quantify the effect of self-supervised pretraining, models initialized from encoders pretrained with different masking ratios were compared against a baseline model trained from scratch, i.e., without pretraining.

Figure 6 shows the evolution of the training and validation losses for the three stiffness components. Across all masking ratios, the fine-tuning process exhibits stable optimization behavior, with both losses decreasing consistently throughout training. A clear and systematic performance gap emerges when comparing pretrained models with the non-pretrained baseline. For all stiffness components and across all masking configurations, the pretrained models achieve substantially lower prediction errors than the model trained without pretraining. This result indicates that the latent representation learned during self-supervised pretraining provides an effective inductive structure for predicting texture-dependent elastic properties.

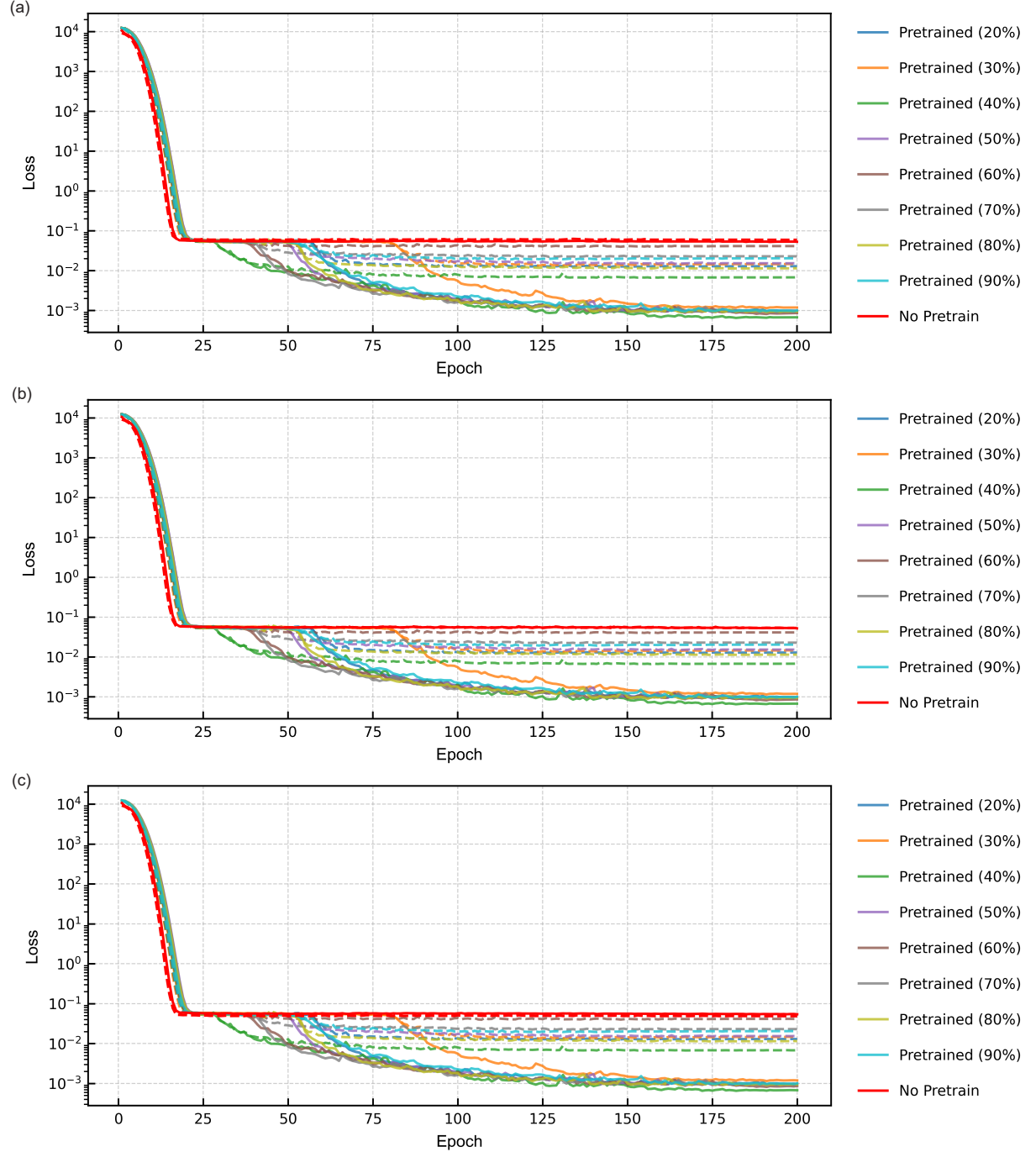


Figure 6: Training and validation loss curves for downstream stiffness prediction of (a) \bar{C}_{1111} , (b) \bar{C}_{2222} , and (c) \bar{C}_{3333} under different masking ratios. Solid lines indicate training loss whereas dashed lines indicate validation loss.

A quantitative comparison of predictive accuracy is presented in Fig. 7, which reports the validation R^2 values for the three stiffness components. The baseline model trained from scratch achieves R^2 values below 0.09 across all components. Given that the dataset spans the entire texture hull, resulting in pronounced anisotropy and highly nontrivial stiffness variations, such limited performance is expected in the absence of informative prior structural representations.

In contrast, all pretrained configurations achieve substantially higher predictive accuracy, even under the data-limited conditions of this downstream task. Among them, the model pretrained with a masking ratio of 40% attains the best overall performance, with validation R^2 values exceeding 0.8 for all three stiffness components. These results highlight the effectiveness of self-supervised pretraining in providing informative latent representations.

In summary, three key observations can be drawn from these results. First, self-supervised pretraining yields latent representations that transfer effectively to elastic property prediction. Second, the masking ratio influences the expressiveness and utility of the learned embedding, leading to measurable differences in downstream accuracy. Third, the foundation-model pretraining strategy results in a substantial improvement in regression performance compared to models trained without pretraining, underscoring its importance for data-efficient microstructure–property learning.

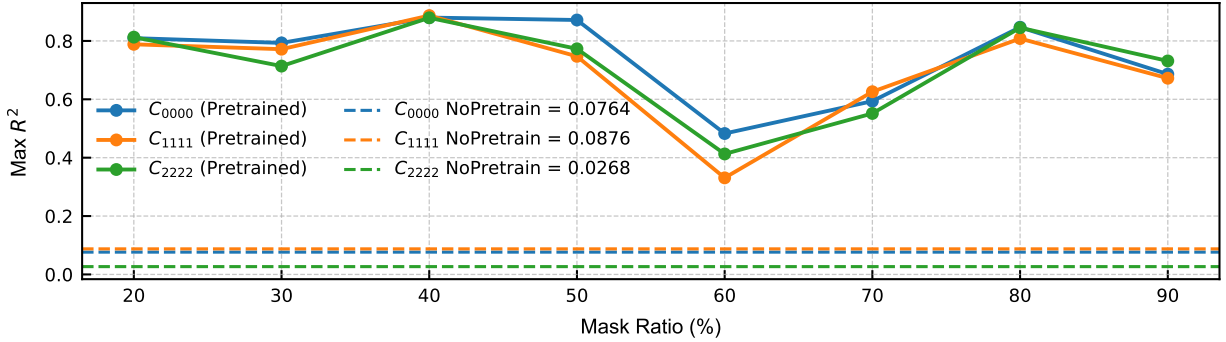


Figure 7: Validation R^2 scores for predicting the stiffness components \bar{C}_{1111} , \bar{C}_{2222} , and \bar{C}_{3333} using models trained with and without self-supervised pretraining. Results are shown for pretrained encoders with different masking ratios.

3.3 Downstream task II: nonlinear response prediction

This downstream task evaluates the transferability of the pretrained encoder by assessing its ability to infer ODMN parameters during the offline training stage and to predict nonlinear mechanical responses during the online prediction stage. Accordingly, the evaluation comprises two complementary aspects. The first focuses on the fine-tuning behavior of the pretrained encoder when coupled with the ODMN. The second examines the accuracy of the inferred ODMNs in predicting nonlinear stress-strain responses for previously unseen microstructures.

During the offline stage, the pretrained encoder was integrated with the ODMN and optimized in an end-to-end manner to infer the ODMN parameters that approximate the homogenized stiffness responses used for supervised training. Pretrained encoders with masking ratios ranging from 20% to 90% were considered, together with an additional baseline model trained entirely from scratch.

The training curves shown in Fig. 8 demonstrate smooth and stable convergence for all configurations. Notably, although the model trained from scratch attains the lowest training error, it exhibits the largest validation error among all cases. This behavior reflects overfitting induced by the absence of pretrained structural priors. Without pretraining, the encoder learns a representation space that is weakly aligned with the physically meaningful manifold of microstructural features, allowing excessive adaptation to the supervised samples and resulting in poor generalization.

The validation performance further underscores the importance of pretraining. As summarized in Fig. 9, the model pretrained with a masking ratio of 40% achieves the lowest validation error of 2.4%, whereas the model trained without pretraining yields a substantially higher validation error of 10.8%. These results demonstrate that self-supervised pretraining promotes a structured and stable latent space, which in turn enhances the generalization capability of the inferred ODMN parameters and improves nonlinear response prediction for unseen microstructures.

During the online prediction stage, the pretrained model with a masking ratio of 40% was selected for evaluation, as it demonstrated the best performance during the offline ODMN training stage. Four representative RVEs were constructed for testing, corresponding to Strong-textured-1, Strong-textured-2, Weak-textured-1, and Weak-textured-2, denoted as S1, S2, W1, and W2.

For each microstructure, the trained encoder was used to infer a standalone ODMN, which was subsequently coupled with a crystal plasticity model to predict the uniaxial loading-unloading stress-strain response [16, 17]. Details of the crystal plasticity formulation and the elastic response are provided in A and B, respectively, and the material parameters employed in the simulations are summarized in Table 3. Reference solutions were obtained using DNS based on the DAMASK-FFT solver [16].

The resulting stress-strain responses are presented in Fig. 10. For all four microstructures, the ODMN-predicted curves show excellent agreement with the DNS reference results across both loading and unloading paths. To quantitatively assess the prediction accuracy, two normalized error metrics were adopted following established definitions in the literature [25]. Specifically, the mean relative error characterizes the average deviation between the predicted and DNS stresses over the loading history, while the maximum relative error captures the largest discrepancy observed along the entire loading path. These metrics are defined as

$$\text{mean-relative error} = \frac{\frac{1}{n} \sum_{i=1}^n |P_i^{\text{DNS}} - P_i^{\text{ODMN}}|}{\max_{i=1,\dots,n} |P_i^{\text{DNS}}|} \quad (15)$$

$$\text{max-relative error} = \frac{\max_{i=1,\dots,n} |P_i^{\text{DNS}} - P_i^{\text{ODMN}}|}{\max_{i=1,\dots,n} |P_i^{\text{DNS}}|} \quad (16)$$

Table 2: Relative stress prediction errors of inferred ODMNs under cyclic loading, compared against DNS results.

RVE	S1	S2	W1	W2
mean-relative error (%)	1.26	3.93	0.81	0.69
max-relative error (%)	2.07	8.68	3.99	1.87

The quantitative results are summarized in Table 2. Across all four RVEs, the mean relative error remains below 4%, indicating that the inferred ODMNs reproduce the nonlinear stress response with consistently high accuracy. The largest maximum relative error is observed for RVE S2, reaching 8.68%. This deviation corresponds to a slight discrepancy relative to the DNS reference and is limited in magnitude compared to the overall nonlinear response.

Overall, these results demonstrate that coupling the foundation model with the ODMN enables robust and accurate prediction of nonlinear mechanical responses for previously unseen microstructures spanning a wide range of texture characteristics.

Table 3: Elastic and plastic material parameters for AA6022-T4 [30, 31].

N_s	$h_0^{\text{sl-sl}}$ (GPa)	ξ_∞^α (MPa)	ξ^0 (MPa)	n	a	$\dot{\gamma}_0$ (s $^{-1}$)	h_{int}^α	
12	1.02	266	76	20	3.7	0.001	0	
C_{11} (GPa)			C_{12} (GPa)	C_{44} (GPa)	$h^{\text{sl-sl}}$			
107.3			60.8	28.3	[1, 1, 5.123, 0.574, 1.123, 1.123, 1]			

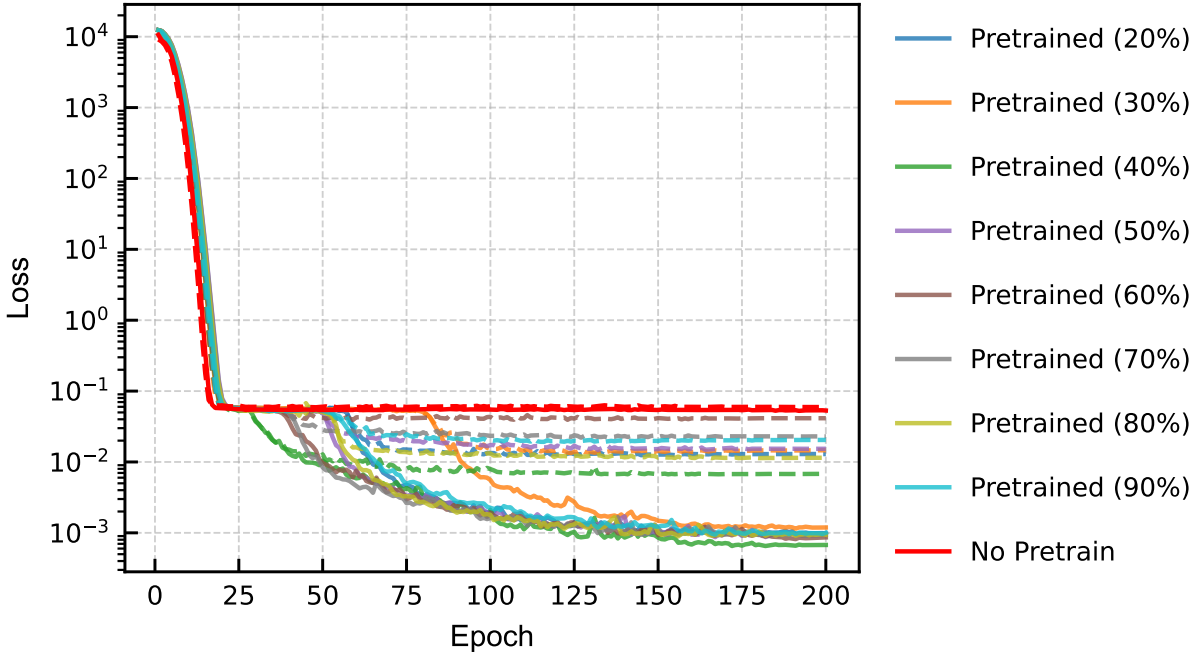


Figure 8: Training and validation loss curves for the downstream task of predicting ODMN parameters under different masking ratios during offline end-to-end fine-tuning. Solid lines denote training loss, whereas dashed lines denote validation loss.

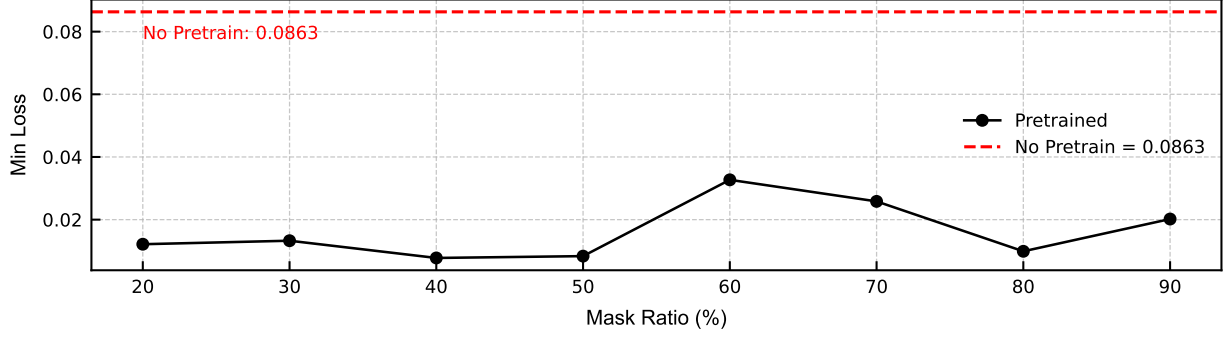


Figure 9: Minimum validation loss for predicting ODMN parameters under different masking ratios during offline end-to-end fine-tuning.

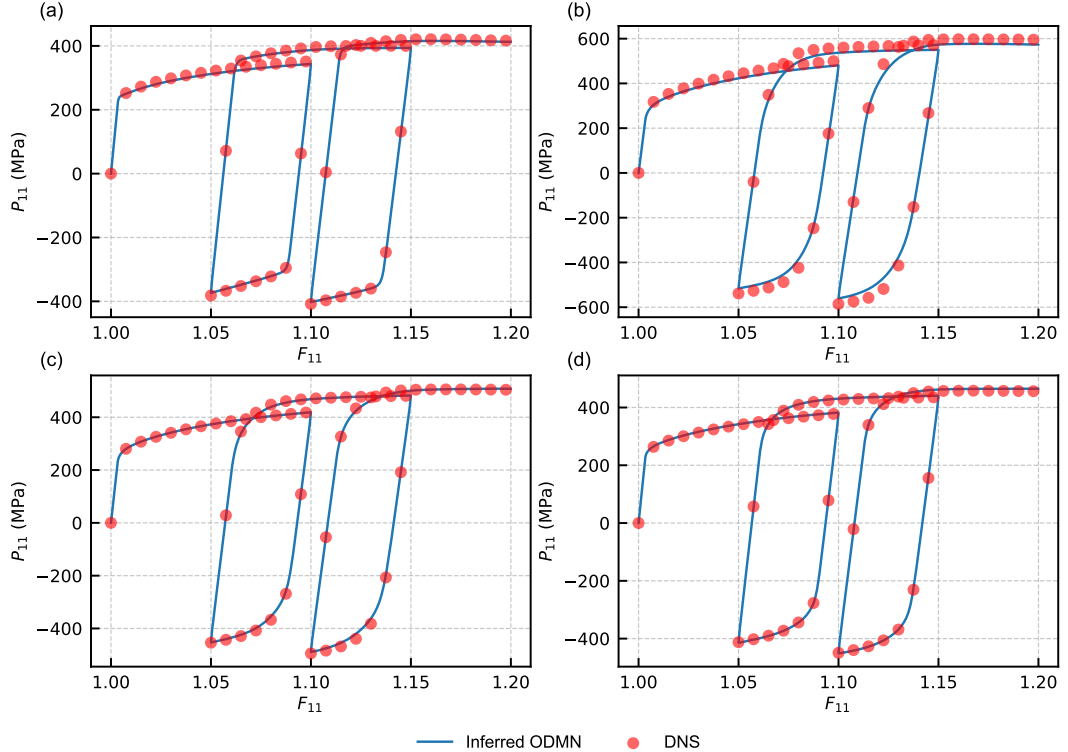


Figure 10: Predicted stress-strain responses obtained from standalone ODMNs inferred for four previously unseen RVEs subjected to cyclic loading. The four cases correspond to (a) S1, (b) S2, (c) W1 and (d) W2.

3.4 Model transferability, interpretability, and current limitations

The capabilities of the proposed foundation model are demonstrated through two downstream tasks characterized by distinct physical settings. In Task I, the objective is to predict the homogenized elastic stiffness components. Although the target response is linear elastic, the input space spans the full crystallographic texture hull, leading to substantial microstructural variability despite the limited availability of labeled data. In Task II, the evaluation is conducted in two stages: an offline training stage and an online prediction stage. During the offline stage, the pretrained encoder is integrated with the ODMN to infer the complete set of ODMN parameters. The model is optimized using labeled homogenized stiffness data to learn the mapping from voxelized microstructures to the ODMN parameterization. Although the training microstructures in Task II cover only a subset of the texture hull, the task remains considerably more challenging, as it requires learning a mapping from microstructure to the corresponding ODMN parameters. During the online prediction stage, the fine-tuned encoder is applied to previously unseen microstructures to infer standalone ODMNs, which subsequently perform nonlinear extrapolation through crystal-plasticity-based homogenization. Task II thus showcases both the transferability of the pretrained encoder and the capability of the inferred ODMNs to generalize beyond the linear training regime and perform nonlinear mechanical extrapolation.

To further elucidate the role of pretraining, a non-pretrained encoder was included as a baseline in both downstream tasks. Across all masking ratios, the non-pretrained encoder consistently exhibits inferior predictive accuracy compared to its pretrained counterparts. A particularly instructive behavior is observed in Task II: the model trained from scratch attains lower training errors but significantly higher validation errors than the pretrained model. This discrepancy reflects a fundamental aspect of representation learning. In the absence of pretraining, the encoder operates in an unconstrained representation space and adapts excessively to the supervised samples, resulting in pronounced overfitting and limited generalization. Self-supervised pretraining, by contrast, organizes the latent space into a physically structured manifold that captures essential microstructural statistics. Although this implicit constraint may slow the reduction of training loss, it provides a valuable inductive bias that steers optimization toward stable, transferable solutions. Such behavior is particularly important in materials informatics, where labeled data are inherently scarce and generalization to previously unseen microstructures is essential.

Despite these encouraging results, the present foundation model is subject to several well-defined scope limitations. Specifically, the current pretraining corpus is restricted to FCC crystal, with texture variations confined to the crystallographic texture hull and grains assumed to be equiaxed. Future work will extend the pretraining dataset to incorporate morphological texture, including grain-shape anisotropy, elongated grains, and direction-dependent microstructural features. Moreover, extending the framework to incorporate experimentally measured microstructures—particularly those associated with additive manufacturing and other process-driven routes—would facilitate a more realistic representation of microstructural heterogeneity and further strengthen the robustness and practical applicability of the proposed model.

4 Conclusions

This study introduced a three-dimensional polycrystal foundation model pretrained on a large corpus of FCC microstructures whose crystallographic orientations span the texture hull. Through a self-supervised masked reconstruction strategy with masking ratios ranging from 20% to 90%, the encoder was trained on 100,000 voxel-based microstructures and learned a physically meaningful latent representation. The resulting latent distribution exhibits an approximately uniform circular topology, indicating that the pretrained encoder provides a smooth and isotropic embedding of the entire pretraining dataset.

The effectiveness of the foundation model was demonstrated through two downstream tasks characterized by distinct physical settings. In Task I, the pretrained encoder was employed as a feature extractor for homogenized stiffness prediction, consistently achieving higher accuracy than the non-pretrained baseline across all masking ratios. In Task II, the encoder was integrated with the ODMN to infer complete sets of ODMN parameters for nonlinear constitutive modeling. In this setting, pretraining consistently reduced the prediction error of the inferred ODMN parameters, while the inferred ODMNs enabled accurate nonlinear response prediction for previously unseen microstructures through crystal-plasticity-based homogenization.

Collectively, these results demonstrate that the proposed foundation model exhibits strong transferability and learns a physically structured latent representation of polycrystalline microstructures. Such characteristics are particularly advantageous in data-scarce scientific regimes, where labeled microstructural data are costly to acquire and physics-consistent generalization is critical. Moreover, the foundation model is naturally amenable to integration with experimentally derived datasets. By serving as a latent-space bridge, it enables limited experimental observations to inform microstructure–property inference, thereby strengthening the linkage between physical measurements and model predictions.

Acknowledgements

This work is supported by the National Science and Technology Council, Taiwan, under Grant 111-2221-E-002-054-MY3, 112-2221-E-007-028, and 114-2221-E-002-010-MY3. We are grateful for the computational resources and support from the NTUCE-NCREE Joint Artificial Intelligence Research Center and the National Center of High-performance Computing (NCHC). The authors also wish to thank José Niño and Oliver K. Johnson for their valuable assistance with the implementation of the hierarchical simplex sampling and texture hull framework.

A Phenomenological Crystal Plasticity Model

In this study, a phenomenological crystal plasticity model is employed as the local constitutive law in ODMN during online prediction stage. The model follows the formulation implemented in DAMASK and neglects deformation twinning [16]. Plastic deformation is described by the plastic velocity gradient \mathbf{L}_p , which is obtained from the accumulated shear contributions of all slip systems α :

$$\mathbf{L}_p = \sum_{\alpha} \dot{\gamma}^{\alpha} (\mathbf{s}_s^{\alpha} \otimes \mathbf{n}_s^{\alpha}) \quad (17)$$

where \mathbf{s}_s^{α} and \mathbf{n}_s^{α} denote the slip direction and slip-plane normal, respectively, and $\dot{\gamma}^{\alpha}$ is the slip rate of system α .

The slip resistance ξ^{α} evolves according to a hardening law that governs its transition from an initial value ξ_0^{α} toward a saturation level ξ_{∞}^{α} . Its evolution is expressed as

$$\dot{\xi}^{\alpha} = h_0^{s-s} (1 + h_{\text{int}}^{\alpha}) \times \sum_{\alpha'}^{N_s} \left| \dot{\gamma}^{\alpha'} \right| \left| 1 - \frac{\xi^{\alpha'}}{\xi_{\infty}^{\alpha'}} \right|^a \text{sgn} \left(1 - \frac{\xi^{\alpha'}}{\xi_{\infty}^{\alpha'}} \right) h^{\alpha\alpha'} \quad (18)$$

where N_s is the total number of slip systems and $h^{\alpha\alpha'}$ represents latent hardening interactions.

The slip rate for each system is given by flow rule that depends on the resolved shear stress τ^{α} and the slip resistance ξ^{α} :

$$\dot{\gamma}^{\alpha} = \dot{\gamma}_0^{\alpha} \left| \frac{\tau^{\alpha}}{\xi^{\alpha}} \right|^n \text{sgn}(\tau^{\alpha}) \quad (19)$$

The resolved shear stress τ^{α} is calculated using Schmid's law and the Mandel stress \mathbf{M}^p :

$$\tau^{\alpha} = \mathbf{M}^p \cdot (\mathbf{s}^{\alpha} \otimes \mathbf{n}^{\alpha}) \quad (20)$$

B Generalized Hooke's law

In this study, the elastic response within the crystal plasticity used in the ODMN formulation is described by the generalized form of Hooke's law. This constitutive relation links the second Piola–Kirchhoff stress tensor \mathbf{S} to the Green–Lagrange strain tensor \mathbf{E} through the fourth-order elasticity tensor \mathbb{C} :

$$\mathbf{S} = \mathbb{C} : \mathbf{E}. \quad (21)$$

Here, \mathbf{S} denotes the second Piola–Kirchhoff stress, \mathbb{C} is the fourth-order elasticity tensor characterizing the material's elastic moduli, and \mathbf{E} is the Green–Lagrange strain tensor. The symbol $:$ denotes the double contraction between two tensors.

The Green–Lagrange strain is expressed in terms of the elastic deformation gradient \mathbf{F}^e as

$$\mathbf{E} = \frac{1}{2} ((\mathbf{F}^e)^T \mathbf{F}^e - \mathbb{I}), \quad (22)$$

where \mathbf{F}^e represents the elastic part of the deformation gradient and \mathbb{I} is the second-order identity tensor.

Declarations

The authors declare that there are no competing interests.

Author Contributions

Conceptualization and Project Administration: All authors. Investigation and methodology: Ting Ju Wei. Writing—Original Draft: Ting Ju Wei. Review & Editing: All authors. Resources and Funding Acquisition: Chuin-Shan Chen. These author contributions are defined according to the CRediT contributor roles taxonomy.

References

- [1] S Amir H Motaman, Franz Roters, and Christian Haase. Anisotropic polycrystal plasticity due to microstructural heterogeneity: A multi-scale experimental and numerical study on additively manufactured metallic materials. *Acta Materialia*, 185:340–369, 2020.
- [2] Mohammad S Khorrami, Jaber R Mianroodi, Nima H Siboni, Pawan Goyal, Bob Svendsen, Peter Benner, and Dierk Raabe. An artificial neural network for surrogate modeling of stress fields in viscoplastic polycrystalline materials. *npj Computational Materials*, 9(1):37, 2023.
- [3] Minyi Dai, Mehmet F Demirel, Yingyu Liang, and Jia-Mian Hu. Graph neural networks for an accurate and interpretable prediction of the properties of polycrystalline materials. *npj Computational Materials*, 7(1):103, 2021.
- [4] Yu-Chun Liu, Chang-Kai Yeh, Shao-Pu Tsai, and Po-Yen Tung. Learning crystallographic orientations from electron backscatter diffraction patterns using variational autoencoder. *Cell Reports Physical Science*, 6(10), 2025.
- [5] Pierre Belamri, Henry Proudhon, Damien Texier, and David Ryckelynck. Quaternion-based vision-transformer for polycrystalline ebsd scans pre-trained on large-scale synthetic data. *Materials & Design*, page 114599, 2025.
- [6] Jacob Devlin, Ming-Wei Chang, Kenton Lee, and Kristina Toutanova. BERT: Pre-training of deep bidirectional transformers for language understanding. In Jill Burstein, Christy Doran, and Thamar Solorio, editors, *Proceedings of the 2019 Conference of the North American Chapter of the Association for Computational Linguistics: Human Language Technologies, Volume 1 (Long and Short Papers)*, pages 4171–4186, Minneapolis, Minnesota, June 2019. Association for Computational Linguistics.
- [7] Alec Radford, Jeffrey Wu, Rewon Child, David Luan, Dario Amodei, Ilya Sutskever, et al. Language models are unsupervised multitask learners. *OpenAI blog*, 1(8):9, 2019.
- [8] Ting-Ju Wei and Chuin-Shan Chen. Foundation model for composite microstructures: Reconstruction, stiffness, and nonlinear behavior prediction. *Materials & Design*, 257:114397, 2025.
- [9] Oliver K Johnson and Christian Kurniawan. An efficient algorithm for generating diverse microstructure sets and delineating properties closures. *Acta materialia*, 147:313–321, 2018.
- [10] José Niño and Oliver K Johnson. Evolution of crystallographic texture and grain boundary network structure during anisotropic grain growth. *Computational Materials Science*, 240:113023, 2024.
- [11] David T Fullwood, Stephen R Niezgoda, Brent L Adams, and Surya R Kalidindi. Microstructure sensitive design for performance optimization. *Progress in Materials Science*, 55(6):477–562, 2010.
- [12] Tony Fast, Marko Knezevic, and Surya R Kalidindi. Application of microstructure sensitive design to structural components produced from hexagonal polycrystalline metals. *Computational Materials Science*, 43(2):374–383, 2008.
- [13] Oliver K Johnson and Christopher A Schuh. Texture mediated grain boundary network design in two dimensions. *Journal of Materials Research*, 31(9):1171–1184, 2016.
- [14] Michael A Groeber and Michael A Jackson. Dream. 3d: a digital representation environment for the analysis of microstructure in 3d. *Integrating materials and manufacturing innovation*, 3(1):56–72, 2014.
- [15] Ashish Vaswani, Noam Shazeer, Niki Parmar, Jakob Uszkoreit, Llion Jones, Aidan N Gomez, Łukasz Kaiser, and Illia Polosukhin. Attention is all you need. *Advances in neural information processing systems*, 30, 2017.
- [16] F. Roters, M. Diehl, P. Shanthraj, P. Eisenlohr, C. Reuber, S.L. Wong, T. Maiti, A. Ebrahimi, T. Hochrainer, H.-O. Fabritius, S. Nikolov, M. Friák, N. Fujita, N. Grilli, K.G.F. Janssens, N. Jia, P.J.J. Kok, D. Ma, F. Meier,

E. Werner, M. Stricker, D. Weygand, and D. Raabe. Damask – the düsseldorf advanced material simulation kit for modeling multi-physics crystal plasticity, thermal, and damage phenomena from the single crystal up to the component scale. *Computational Materials Science*, 158:420–478, 2019.

[17] Ting-Ju Wei, Tung-Huan Su, and Chuin-Shan Chen. Orientation-aware interaction-based deep material network in polycrystalline materials modeling. *Computer Methods in Applied Mechanics and Engineering*, 441:117977, 2025.

[18] Zeliang Liu, C. T. Wu, and M. Koishi. A deep material network for multiscale topology learning and accelerated nonlinear modeling of heterogeneous materials. *Computer Methods in Applied Mechanics and Engineering*, 345:1138–1168, MAR 1 2019.

[19] Van Dung Nguyen and Ludovic Noels. Micromechanics-based material networks revisited from the interaction viewpoint; robust and efficient implementation for multi-phase composites. *European Journal of Mechanics - A/Solids*, 91:104384, 2022.

[20] Van Dung Nguyen and Ludovic Noels. Interaction-based material network: A general framework for (porous) microstructured materials. *Computer Methods in Applied Mechanics and Engineering*, 389:114300, 2022.

[21] Ling Wu and Ludovic Noels. Stochastic deep material networks as efficient surrogates for stochastic homogenisation of non-linear heterogeneous materials. *Computer Methods in Applied Mechanics and Engineering*, 441:117994, 2025.

[22] Dongil Shin, Ryan Alberdi, Ricardo A Lebensohn, and Rémi Dingreville. Deep material network via a quilting strategy: visualization for explainability and recursive training for improved accuracy. *npj Computational Materials*, 9(1):128, 2023.

[23] Sebastian Gajek, Matti Schneider, and Thomas Böhlke. On the micromechanics of deep material networks. *Journal of the Mechanics and Physics of Solids*, 142:103984, 2020.

[24] Wen-Ning Wan, Ting-Ju Wei, Tung-Huan Su, and Chuin-Shan Chen. Decoding material networks: exploring performance of deep material network and interaction-based material networks. *Journal of Mechanics*, 40:796–807, 2024.

[25] Tianyu Huang, Zeliang Liu, CT Wu, and Wei Chen. Microstructure-guided deep material network for rapid nonlinear material modeling and uncertainty quantification. *Computer Methods in Applied Mechanics and Engineering*, 398:115197, 2022.

[26] Jimmy Gaspard Jean, Tung-Huan Su, Szu-Jui Huang, Cheng-Tang Wu, and Chuin-Shan Chen. Graph-enhanced deep material network: multiscale materials modeling with microstructural informatics. *Computational Mechanics*, 75:113–136, 2025.

[27] Ling Wu and Ludovic Noels. Convolutional neural network-based mapping of material micro-structures to deep material networks for non-linear mechanical response prediction. *Computer Methods in Applied Mechanics and Engineering*, 449:118554, 2026.

[28] Wei Dai, Huamiao Wang, Qiang Guan, Dayong Li, Yinghong Peng, and Carlos N Tomé. Studying the micromechanical behaviors of a polycrystalline metal by artificial neural networks. *Acta Materialia*, 214:117006, 2021.

[29] Leland McInnes, John Healy, and James Melville. Umap: uniform manifold approximation and projection for dimension reduction. arxiv. *arXiv preprint arXiv:1802.03426*, 10, 2018.

[30] Timothy J. Barrett and Marko Knezevic. Deep drawing simulations using the finite element method embedding a multi-level crystal plasticity constitutive law: Experimental verification and sensitivity analysis. *Computer Methods in Applied Mechanics and Engineering*, 354:245–270, 2019.

[31] Max-Planck-Institut für Eisenforschung GmbH. Damask documentation: Phenopowerlaw aa6022-t4, 2024. Accessed: 21st June 2024.